

# A new thermography-based approach to early detection of cancer utilizing magnetic nanoparticles theory simulation and in vitro validation

Arie Levy, MSc, Abraham Dayan, PhD, Moshe Ben-David, PhD, Israel Gannot, PhD\*

Department of Biomedical Engineering, Tel Aviv University, Tel Aviv, Israel

Received 29 October 2009; accepted 20 June 2010

## Abstract

This work describes the utilization of tumor-specific magnetic nanoparticles together with an alternating magnetic field as a means to thermally mark a tumor so as to detect it using a thermal imaging system. Experiments were conducted using an in vitro tissue model, an inductive heating system, and an infrared camera. The thermal images, recorded by the infrared camera during the experiments, were analyzed using an algorithm that was developed as part of this work. The results show that small tumor phantoms (diameter of 0.5 mm) that were embedded under the surface of the tissue phantom (up to 14 mm below the surface) can be detected and located, indicating that the proposed method could potentially offer considerable advantages over conventional thermography and other methods for cancer early detection. Nevertheless, several issues should be clarified in future studies before the method can be offered for clinical use.

**From the Clinical Editor:** Tumor-specific magnetic nanoparticles exposed to an alternating magnetic field provide a method to thermally mark a tumor for detection using thermal imaging systems. In-vitro tissue model experiments demonstrated that tumor phantoms of 0.5mm up to 14mm below the surface can be detected and located, indicating that the proposed method could offer considerable advantages over conventional thermography.

© 2010 Elsevier Inc. All rights reserved.

**Key words:** Thermography; Magnetic nanoparticles; Antibody targeting

Cancer is a world epidemic, claiming the lives of more than 500,000 people each year in the United States alone.<sup>1</sup> Early detection of cancer can significantly improve the patient's chances of survival.<sup>2</sup> In most cases cancer is detected using an imaging method [e.g., mammography, computed tomography, magnetic resonance imaging (MRI)]. However, there are several disadvantages associated with the current methods; chief among these are the lack of sufficient sensitivity and specificity, high costs, and significant health risks. Therefore, considerable efforts are being invested to improve the performance of the present imaging modalities.

Thermography was proposed more than five decades ago as a cost-effective tool for early detection of breast cancer.<sup>3</sup> Thermography can detect cancer according to temperature differences on the skin surface as a result of the presence of an embedded cancerous tumor. This temperature increase is generated mainly by increased metabolism and blood perfusion in and around tumors<sup>4</sup> and can be detected using an infrared (IR)

camera, which is utilized for remote measurement of the patient's skin temperature. The thermal images acquired by the IR camera are analyzed by an expert radiologist so as to detect thermal patterns that can indicate the presence of an embedded tumor. The radiologist can also be aided by image analysis tools.

Thermography can offer several considerable advantages<sup>4</sup>: it is radiation and contact free, and it is a relatively low-cost approach. However, thermography has several considerable disadvantages when compared to other early cancer detection methods (e.g., mammography), including its relatively low sensitivity for deep and small tumors,<sup>4</sup> its inability to distinguish tumors from natural "hot spots" (e.g., local inflammation), and its reliance as a subjective method on the radiologist's skills to interpret the IR images. Because of these disadvantages and other factors, thus far thermography has failed to gain full acceptance as a primary tool for cancer screening. Numerous studies have tried to improve thermography performances by using various image analyses, algorithms, and other approaches, such as asymmetry analysis<sup>5</sup> and dynamic thermography.<sup>6</sup> However, tumor-specific thermal markers have not yet been proposed as a means for improving thermography performance.

The current work suggests using tumor-specific magnetic nanoparticles (MNPs) as such thermal markers so as to improve the current tumor detection ability of thermography. MNPs are

No conflict of interest was reported by the authors of this article.

\*Corresponding author: Department of Biomedical Engineering, Tel Aviv University, Levanon St., Tel Aviv 69978, Israel.

E-mail address: [gannot@eng.tau.ac.il](mailto:gannot@eng.tau.ac.il) (I. Gannot).

1549-9634/\$ – see front matter © 2010 Elsevier Inc. All rights reserved.  
doi:10.1016/j.nano.2010.06.007

biocompatible particles that are already utilized in various medical fields including MRI contrast enhancement,<sup>7</sup> drug delivery,<sup>8</sup> and local hyperthermia treatment.<sup>9,10</sup> These particles have several unique properties, the one most relevant to the scope of this work being their ability to generate heat when subjected to an alternating magnetic field (AMF); this heat generation is the result of two dominant thermal losses,<sup>10</sup> Brown losses and Néel losses. Brown losses is a term for heat generation by friction as a result of mechanical rotation of the particles by the AMF. Néel losses is a term for heat generation caused by rotation of the magnetic moment inside the particle. Other effects such as “hysteresis losses” and “eddy current losses” are neglected in this particle size range.

In addition to these unique properties, tumor-specific targeting of such MNPs for the purpose of local hyperthermia treatment was demonstrated in numerous *in vivo* studies. Such targeted delivery of MNPs to a tumor site could be accomplished by using one of three main approaches: physical targeting, passive targeting, and active targeting.<sup>11,12</sup> The most relevant targeting technique for the scope of this work is active targeting, according to which targeting molecules (e.g., antibodies) are attached to the surface of the MNP; these molecules have high affinity to a certain targeting site at the targeted tumor tissue (e.g., antigen present on the cell membrane) and low affinity to healthy tissue. As a result, once these particles are delivered to the patient, they are specifically accumulated at the tumor site. Shinkai et al. have demonstrated active targeting of MNPs conjugated with G250 antibody to renal cell carcinoma tumors; this antibody specifically binds to MN antigen, a known tumor-associated antigen that is overexpressed in many types of human renal cell carcinoma.<sup>13</sup> DeNardo et al. have also demonstrated active targeting of MNPs to human breast cancer tumor using <sup>111</sup>In-chimeric L6 monoclonal antibody.<sup>14</sup> Le et al. have demonstrated MNP targeting to glioma cells.<sup>15</sup>

Based on these previously achieved results, the current work suggests utilizing antibody-conjugated MNPs as a tumor-specific thermal marker. According to the proposed approach, tumor-specific MNPs will be injected into the patient’s bloodstream as a solution; each particle will be coated with tumor-specific molecules (e.g., antibodies), so it will have high affinity for tumor cells. Once the MNP solution has been injected into the bloodstream, the MNPs will accumulate at the tumor site (if it exists in the patient’s body), while the remaining MNPs will be removed by the liver. At the next stage the patient will be subjected to AMF, elevating the tumor temperature by a few degrees (~2 K) and creating a local heat source at the tumor site. As a result, the skin temperature above the tumor will be changed; these changes will be detected using an IR camera and will be processed by a dedicated image processing algorithm so as to indicate the presence of the tumor and estimate its location. Because the heat source at the tumor site can be activated and deactivated by external control, it can induce time-varying patterns on the tissue surface that can be clearly distinguished from other, constant and nonpathological temperature patterns. In other words, the MNPs, located at the tumor site, could be utilized as a “thermal beacon” to detect and locate the tumor; accordingly, this proposed method is termed thermal beacon thermography or TBT.

The specific objectives of this research were (1) to develop a procedure that detects and locates an embedded tumor inside a tissue by analyzing temperature changes at the tissue surface, as were captured using an IR camera during heat source activation; (2) to verify the proposed approach by using *in vitro* experimental setups; and (3) to quantify the proposed approach performance in term of accuracy, sensitivity, and specificity.

## Methods

### Experimental setups

To verify the proposed concept and to achieve our research objectives, we used two separate experimental setups combined with several different experiment protocols. Both of the setups utilized an embedded heat source to simulate a magnetically marked tumor while an IR camera recorded the surface temperature of the tissue phantom. Experimental setup 1 was used to accurately and repeatedly simulate a wide range of possible scenarios; experimental setup 2 provided a more realistic simulation of one specific clinical situation, utilizing porcine tissue and MNPs, so as to demonstrate the proposed tumor detection concept.

### Experimental setup 1

This setup allowed an accurate and repeatable simulation of a wide range of tumor depths and tumor emission power values; this was accomplished by utilizing an electrical heat source as tumor phantom and micrometric translation stage for precise control of the tumor depth (Figure 1). The healthy surrounding tissue was simulated using a cylindrical glass cup (diameter 70 mm, height 40 mm), which was filled with aqueous gel (Aquasonic, Parker Laboratories Inc). The gel-filled cup was covered from the top by a polyurethane film (diameter 0.5 mm). The magnetically marked tumor tissue was simulated by a 1-k $\Omega$  surface-mounted resistor measuring 1  $\times$  1.5  $\times$  0.4 mm. This resistor was utilized as a controllable point heat source. The resistor was connected to a direct-current (DC) power supply by two 0.1-mm insulated copper wires. The resistor and its wires were mounted on a 0.6-mm glass fiber (for location of the resistor inside the gel) and were inserted into the aqueous gel through a small hole at the bottom of the glass cup. The DC power value was set to simulate a specific scenario with a specific tumor volume, MNP concentration, and specific heat absorption (SAR) of the MNPs. The DC power value is given by Eq 1:

$$P_a = S_p \times V \times C \quad (1)$$

where

$P_a$  is the amount of dissipated power (in watts, W) at the tumor site for the specific simulated scenario;

$S_p$  is the SAR of the MNP (W/g);

$V$  is the volume of the tumor (m<sup>3</sup>); and

$C$  is the MNP concentration (g/m<sup>3</sup>) at the tumor site.

Table 1 describes several clinically possible heat source power values for a spherically shaped tumor as a function of its diameter and SAR of the MNPs. The SAR ( $S_p$ ) values were set according to several related studies.<sup>9,13,16</sup> The MNP

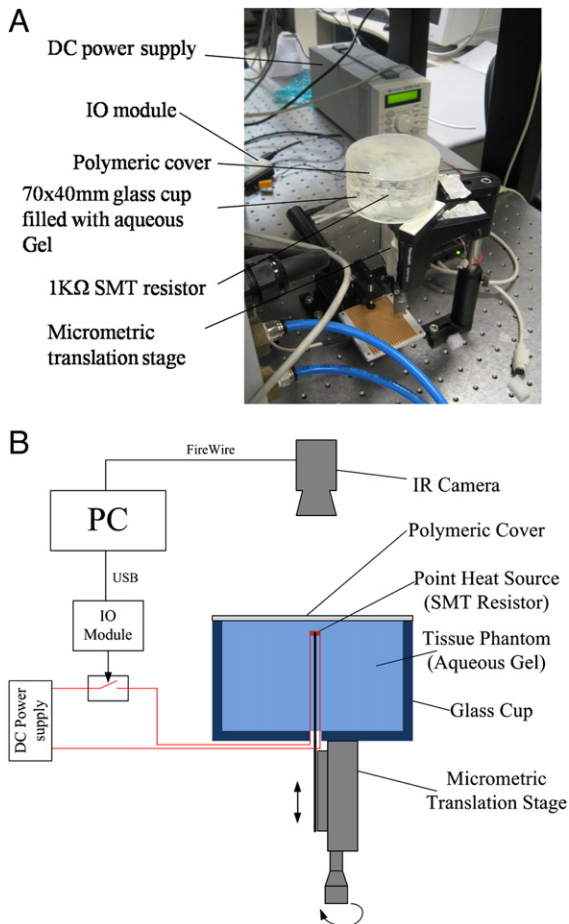


Figure 1. An actual image (A) and a schematic representation (B) of experimental setup 1.

Table 1

Total dissipated power at the tumor site for several combinations of SAR values of MNPs and tumor diameter for spherically shaped tumors as a function of tumor diameter

Diameter (mm)	Total dissipated power at the tumor site, $P_a$ (mW)		
	$S_p = 100$ (W/g)	$S_p = 400$ (W/g)	$S_p = 900$ (W/g)
1	0.41	1.65	3.72
2	3.30	13.22	29.74
3	11.15	44.62	100.39
4	26.44	105.76	237.96
5	51.64	206.56	464.76

concentration value was set to 7.89 mg/mL, a MNP concentration value that was achieved in an in vivo experiment utilizing antibody targeting.<sup>13</sup>

As can be seen in Table 1, the possible heat source power for tumors smaller than 5 mm ranges between 0.4 and 465 mW; accordingly, the heat source power values (resistor heat losses), used during the experiments, were in this values range.

The glass fiber was attached to a vertical micrometric translation stage, which enabled us to accurately set the resistor depth inside the aqueous gel. The point heat source (the resistor)

was turned on and off by an electromagnetic relay that was controlled by an input/output (I/O) module (NI USB-6008; National Instruments, Austin, Texas). The I/O module was connected to a personal computer (PC) by a USB connection. The amount of the power emitted from the resistor during the experiment was set by presetting the DC source voltage. An IR camera (ThermoVision A40, FLIR, Boston, Massachusetts) was placed 50 cm above the phantom surface to capture and record its temperature during the experiments. The IR images that were captured during the experiments were transferred to the PC by a FireWire connection and were recorded on the PC hard drive. The images were later analyzed using MATLAB (Mathworks, Natick, Massachusetts) application. The experiments were automatically conducted by a LabView (National Instruments, Austin, Texas) application.

### Experimental setup 2

The first experimental setup did not simulate the effect of AMF on a tissue and did not completely simulate the thermal behavior of the tissue; therefore, a second experimental setup was used (Figure 2). Experimental setup 2 utilized MNPs and an AMF generator to simulate a specific clinical scenario. An industrial 300-kHz, 3-kW inductive heating system (HFI3kW; RDO Induction LLC, Washington, New Jersey) and a custom-made water-cooled coil generated the AMF. The examined tissue (tissue phantom) was a square of porcine tissue ( $40 \times 40 \times 33$  mm) that included 2 mm of skin, 7 mm of subcutaneous fat tissue, and 24 mm of muscle layer. A simulated magnetically marked tumor (tumor phantom) was prepared by suspending MNP solution (5 mg/mL,  $\gamma$ -Fe<sub>2</sub>O<sub>3</sub>, mean diameter 20 nm) in an agar gel, resulting in a small solid cylinder (diameter 4 mm, height 3 mm). The tumor phantom was inserted laterally into the fat layer, 3 mm below the skin surface. Once the AMF was activated, it induced a temperature increase of  $\sim 2$  K at the tumor phantom location. An IR camera (ThermoVision A40, FLIR) was placed 50 cm above the tissue phantom to capture its surface temperature during the experiment. The camera was connected to a PC by a FireWire connection. The IR images were recorded on the PC hard drive and were later analyzed using MATLAB.

### Protocol

To estimate the performance in term of sensitivity, specificity, and accuracy as a function of heat dissipation power and tumor depth, several experimental sets were performed, each set including numerous individual experiments. Each individual experiment simulated an individual tumor detection session and included the following stages:

1. A reference set of images were recorded for 5 seconds, before the heat source (electrical or magnetic) was activated.
2. The heat source was activated while the camera kept on recording the tissue surface temperature for an additional 100 seconds (i.e., data set).
3. The IR images sequence was stored on the PC hard drive for offline processing by the dedicated detection algorithm (to be described later).

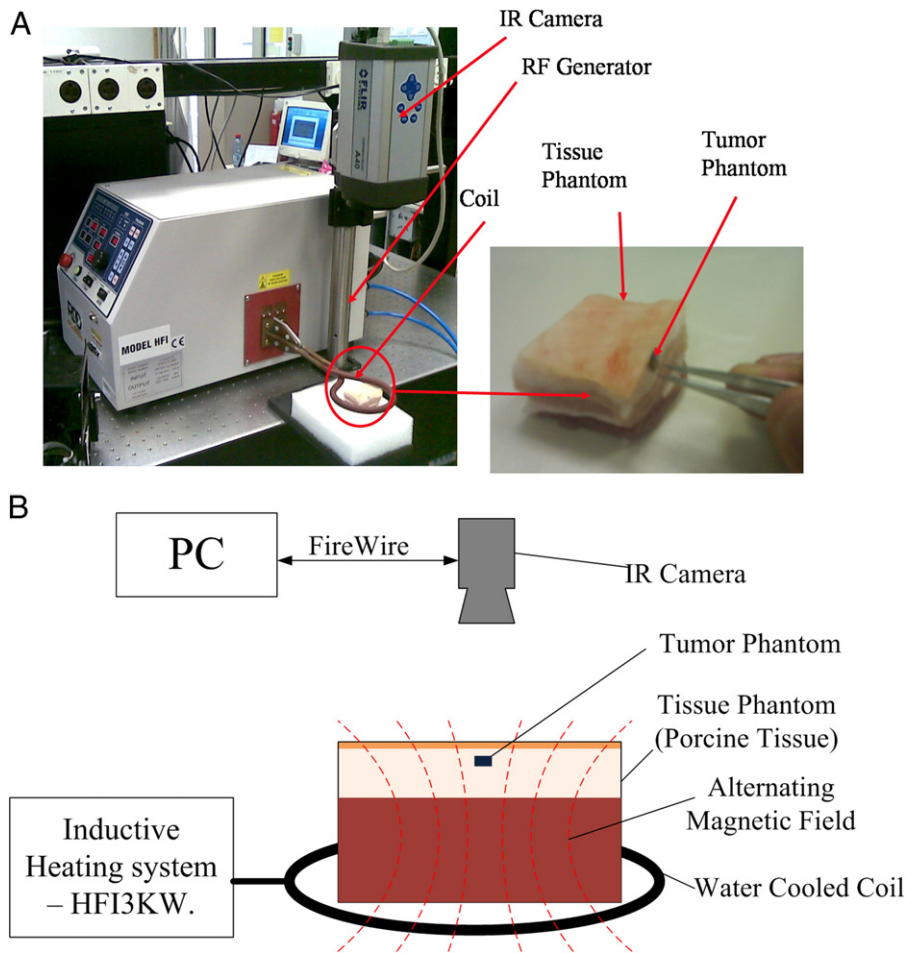


Figure 2. An actual image (A) and a schematic representation (B) of experimental setup 2.

4. The heat source was turned off for a cooling period before the next individual experiment. For both the data and the reference sets, all captured images were averaged and stored once every 1 second. This protocol was implemented using a dedicated LabView application.

The following experiments sets were performed:

1. *Depth scan experiments set.* The purpose of this experimental set is to determine the dependency between the tumor depth and the algorithm performance. This set was performed with experimental setup 1 and included a series of individual experiment with a tumor phantom embedded at different depths, ranging from 1 mm to 14 mm with 1-mm intervals, while maintaining a constant emitted power. This set was repeated for three different emitted power values: 5, 50, and 400 mW. For statistical evaluation purpose, 20 separate individual experiments were performed for each combination of depth and power. The data obtained for every depth and power combination were used for evaluation of depth estimation bias and standard deviation, in addition to tumor detection sensitivity. The tumor detection sensitivity is defined as the ability of the detection algorithm to detect the presence of a tumor in case a tumor is actually present in the tissue;

the tumor detection sensitivity was evaluated for each specific scenario (i.e., each combination of tumor depth and power) by dividing the number of times in which a tumor was correctly detected by the total number of experiments performed with the specific scenario.

2. *Power scan experiment set.* The purpose of this experimental set is to determine the dependency between the emitted power and the algorithm performance. This set was performed similarly to the depth scan set; however, in this case the depth remained constant at 1 mm during the experimental series while the emitted power was changed from 1 to 5 mW with 1-mW intervals.

3. *Specificity test experiments set.* The purpose of this experimental set is to measure the algorithm specificity by performing 150 individual experiments using experimental setup 1. To simulate a scenario of a healthy tissue that does not contain any tumor, all of the experiments were performed without activating the heat source. The recorded sequences were analyzed using the detection algorithm so as to detect the presence of a tumor. The specificity is defined as the ability of the detection algorithm to determine that a tumor does not exist at the tissue in case it does not exist. The specificity was evaluated by dividing the number of times in which the

Table 2  
High-sensitivity threshold parameter set

Parameter	Value
$T_{hs}$	$5.63 \times 10^{-3}$ (K)
$T_m$	0.9

Table 3  
High-specificity threshold parameter set

Parameter	Value
$T_{hs}$	$14.71 \times 10^{-3}$ (K)
$T_m$	0.9

algorithm correctly determined that a tumor does not exist inside the tissue by the total number of experiments.

4. *AMF experiments set.* The purpose of this experimental set is to provide preliminary concept validation using experimental setup 2. During the experiment 20 individual experiments were performed with a 10-minute interval between each individual experiment. The recorded sequence data obtained from all of the experiments were analyzed to detect the presence of a tumor and to estimate its location. The estimation accuracy (in terms of bias and standard deviation) and the detection specificity were calculated in the same manner as described above.
5. *Training experiments set and threshold values calculation.* As will be described later, two threshold parameters,  $T_{hs}$  and  $T_m$ , were used during the data processing stage to determine whether or not a tumor exists inside the tissue. As described in the algorithm overview section, the parameter  $T_{hs}$  represents the minimal local temperature difference above which a hot spot (a local temperature peak) is suspected to have originated from a tumor; each such hot spot is classified by a separate classification stage. The parameter  $T_m$  represents the minimal relative matching (1, full match; 0, no match) above which a suspect hot spot is regarded as a hot spot that originated from a thermally marked tumor.

These threshold values were calculated by a separate experimental set (i.e., training experiments set) done with several worst-case scenarios of tumor depth and power. The threshold values determine the detection algorithm performance in terms of specificity and sensitivity. Because there is a clear tradeoff between specificity and sensitivity, two separate threshold sets of  $T_{hs}$  and  $T_m$  parameters were used during data analysis:

1. *High-sensitivity set.* This threshold values set (Table 2) was calibrated to produce high sensitivity values with lower specificity values.
2. *High-specificity set.* This threshold values set (Table 3) was calibrated to produce high specificity values with lower sensitivity values.

The selection between high-sensitivity and high-specificity sets will be made according to the particular clinical considerations and the specific application.

### Algorithm description

#### Assumptions

The following assumptions were made for the detection process:

1. Because the system is designed to detect early-stage tumors (i.e., tumors smaller than 5 mm in diameter), and because the temperature pattern at the tissue surface that is generated by such tumors is substantially similar to a pattern generated by a point heat source, the tumor was regarded as a point heat source.
2. The tissue was numerically modeled using numerical simulation software (COMSOL Multiphysics, Burlington, Massachusetts). The Pennes bioheat equation (Eq. 2)<sup>17</sup> was used as the equation system for this simulation:

$$k \nabla^2 T + \rho_b C_b \omega_b (T_a - T) + Q_m + Q_e = \rho \cdot C \cdot \frac{\partial T}{\partial t} \quad (2)$$

where  $T$  represents the tissue temperature (K),  $T_a$  represents the arterial blood temperature (K),  $k$  represents the thermal conductivity of the tissue (W/m/K),  $\omega_b$  represents the blood perfusion rate around the tumor (1/s),  $C_b$  represents the blood specific heat (J/K/G),  $C_t$  represents the tissue specific heat (J/kg · K),  $\rho_b$  represents the blood density (kg/m<sup>3</sup>),  $\rho$  represents the tissue density (kg/m<sup>3</sup>),  $Q_m$  represents the metabolic heat generation (W/m<sup>3</sup>), and  $Q_e$  represents the heat generation (W/m<sup>3</sup>) as a result of external effects (e.g., heat absorption in MNPs).

1. The thermal properties of the tissue were assumed according to the relevant literature<sup>18</sup> as follows: The tissue's thermal conductivity  $k$  was set to 0.37 (W/m/k) for the skin, 0.48 (W/m/k) for the muscle layer, and 0.16 (W/m · K) for the fat layer. The tissue's heat capacity  $C$  was set to 3280 (J/K/G) for the skin, 3870 (J/K/G) for the muscle layer, and 2400 (J/K/G) for the fat layer. The tissue density  $\rho$  was set to 1000 (kg/m<sup>3</sup>) for all layers. In the present study the blood perfusion and the metabolism were set to 0 but can be easily changed for future in vivo experiments.
2. Heat losses through the tissue surface by evaporation and convection were neglected.

#### Algorithm overview

The detection process includes three main stages: preprocessing, hot spot detection, and hot spot classification (Figure 3).

At the preprocessing stage the reference data are averaged and subtracted from the data. Next, the data are filtered to eliminate camera spatial and temporal white noises in addition to slow-changing baseline drift artifact. The spatial and temporal white noises were filtered using linear filters while the baseline drift was filtered by estimation and subtraction of the baseline drift noise.

The resulting preprocessed data reveal hot spots that may or may not have originated from an embedded tumor. To determine this, each hot spot is first detected (by the hot spot detection algorithm) and then classified. If the classification process

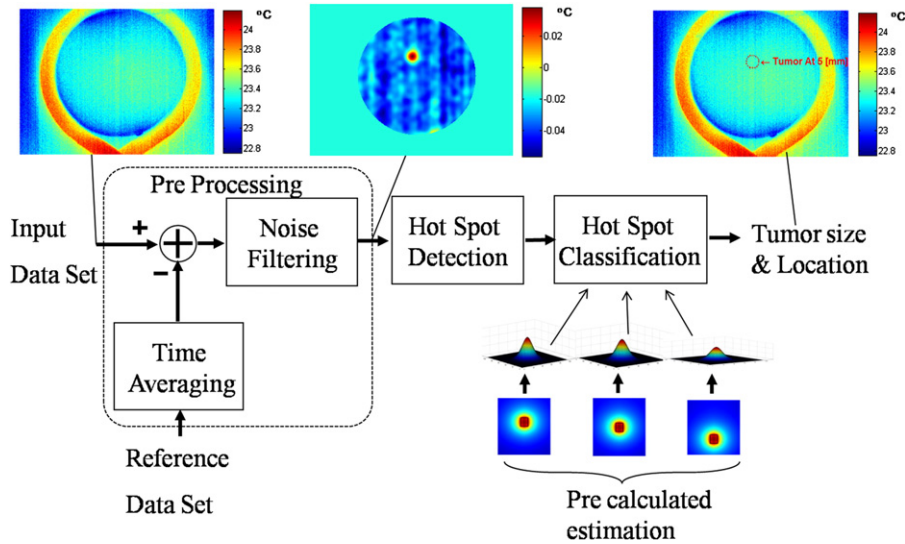


Figure 3. Schematic illustration of the main stages in the detection algorithm.

determines that the hot spot originated from an embedded tumor, its depth is estimated.

The detection is based on two main features of “true” hot spot (i.e., hot spot that originated from a tumor): (a) Their peak is usually a local maximum point at the preprocessed data, and (b) their peak is usually higher than the peak of other local maximum points. Therefore, the algorithm searches for any local maximum point inside the region of interest and marks only the ones with amplitude values larger than a predetermined hot spot detection threshold,  $Ths$ . The hot spot detection threshold  $Ths$  was predetermined according to the training experiments set (described above).

The classification and depth estimation is based on comparison between the hot spot data (as were obtained during the acquisition) and a set of precalculated numerical predictions of the surface temperature (calculated using COMSOL Multiphysics); each prediction is calculated for a different tumor depth. If at least one of these predictions matches the hot spot data beyond a predetermined matching threshold,  $Tm$ , the algorithm determines that the hot spot originated from an embedded marked tumor and estimates its depth according to the prediction that has produced the best matching value. The matching threshold value,  $Tm$ , was predetermined according to the training experiments set (described above). The matching value calculation is based on the mean square error criteria and is calculated according to Eq 3:

$$Mv(d) = 1 - \frac{\sum_t w(t) \cdot \sum_x \sum_y (r(x,y,t) - p(x,y,t,d))^2}{\sum_t w(t) \cdot \sum_x \sum_y r(x,y,t)^2} \quad (3)$$

where:

$Mv$  (matching value vector) is a vector containing the normalized matching value for each individual predetermined prediction;  
 $r$  (recorded data matrix) is a three-dimensional matrix containing the recorder and preprocessed temperature pattern

at a small area around the hot spot peak for every recorded time slot;

$p$  (prediction matrix) is a four-dimensional matrix that contains the temperature pattern at a small area around the hot spot peak for every recorded time slot ( $t$ ) and for every tumor depth ( $d$ ); and

$w$  (weight vector) is a vector containing the relative weight for each individual time slot. The weight values for earlier time slots are generally lower than those of the later ones.

To achieve greater accuracy than the prediction depths intervals, the matching value vector is interpolated. The estimated depth is then determined according to the location of the maximum point along the interpolated matching value vector (Eq 4).

$$\hat{d} = \operatorname{argmax}(Mv_i) \quad (4)$$

where

$\hat{d}$  is the estimated tumor depth; and

$Mv_i$  is a cubic spline interpolation of the matching value vector ( $Mv$ ).

## Results

### Overview

As was predicted by the numerical simulation, the results shows that the tumor phantom (both the MNPs and the electrical heat source) have produced an asymptotic temperature increase pattern at the tissue surface, with a distinct relation between the tumor depth and the temperature elevation rate at the tissue surface. In general, shallow tumors produced a more rapid temperature increase pattern than deeper ones. In addition, the deeper tumor produced wider area hot spots compared to the shallower ones; this relation was also predicted by the simulation. These differences have allowed the algorithm to detect correctly the presence of the embedded tumor phantom

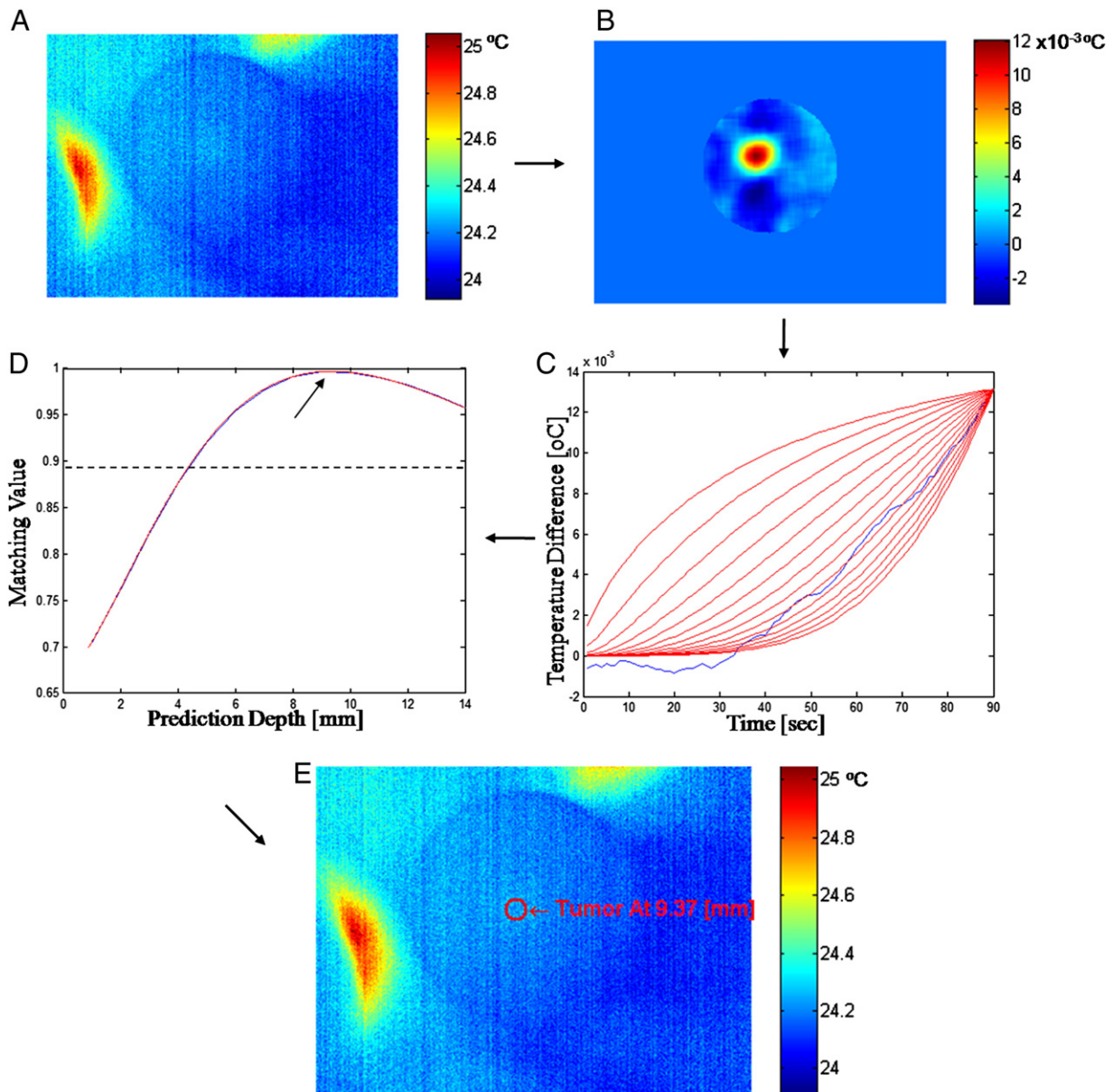


Figure 4. Description of several stages during the tumor detection process, including (A) the last time frame at the original capture IR image, (B) the preprocessed image of the same frame, (C) the temperature of the peak point at the hot spot vs. time for the captured preprocessed data (in blue) and for several numerical prediction (in red), (D) matching values graph as calculated according to the numerical predictions, and (E) the original image with the location of the tumor and its depth marked on it. (Note: Degrees K = Degrees C + 273.15.)

and to provide an accurate estimation of its location; Figure 4 describes various stages during such detection and depth estimation of a 9-mm embedded tumor phantom.

#### Tumor detection sensitivity as a function of depth

As can be seen in Figure 5, A, the proposed algorithm can detect an embedded tumor with very high sensitivity for most of the scenarios (up to 100% evaluated sensitivity). It should be clarified that these results do not necessarily imply that 100% sensitivity can be achieved in a practical clinical scenario, because several factors, such as blood perfusion and human

errors, were not modeled in this experimental setup. The relationship between the detection sensitivity and the tumor depth is highly nonlinear, with a distinct threshold depth in which the sensitivity descend sharply. The results also shows that the proposed method's tumor detection ability is closely related to the amount of emitted power; embedded tumors that emit 400 mW of heat power can be detected as deep as 14 mm below the tissue surface, whereas embedded tumor that emits 5 mW can be detected only up to 5 mm below the tissue surface.

As can be seen in Figure 5, B, when the “high-specificity” threshold values were used, the result was a reduction of ~1–3 mm in the maximal detection depth: 13 mm for 400 mW,

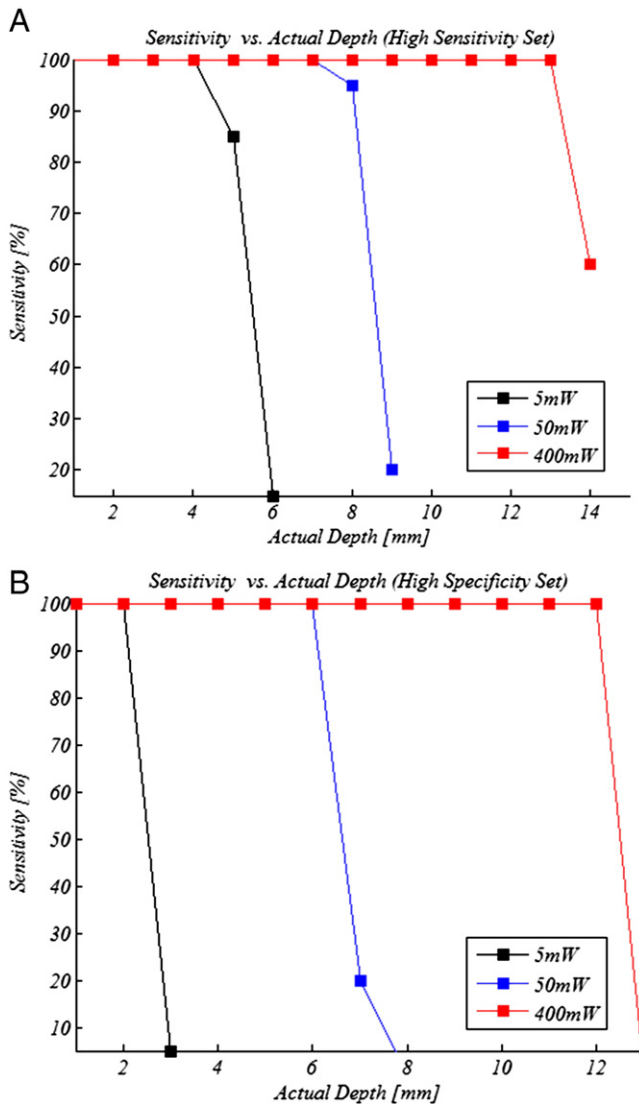


Figure 5. Tumor detection sensitivity as a function of depth, for the high-sensitivity parameters set (A) and high-specificity parameters set (B), each one for three different cases of heat emission power emitted from the tumor phantom: 5 mW (black), 50 mW (blue), and 400 mW (red).

6 mm for the 50 mW, and 2 mm for 5 mW. The sensitivity evaluation values below these maximal depths remained 100%, meaning that the effect was limited only for the higher range of tumor’s depths.

*Depth estimation bias and accuracy as a function of depth*

As can be seen at Figure 6, the depth estimation results for the high-power scenarios (400 mW) were with relative low bias values (0.1–1 mm) and good accuracy values (0.1 and up to 0.7 mm SD); however, for the medium and low-power scenarios (5 mW and 50 mW) there were significant bias values (up to 4.5 mm) and lower accuracy (up to 2 mm SD) for tumors deeper than 4 mm.

As long as the amplitude is substantially strong (i.e., above  $5 \times 10^{-2}$  K), the algorithm performances in terms of sensitivity,

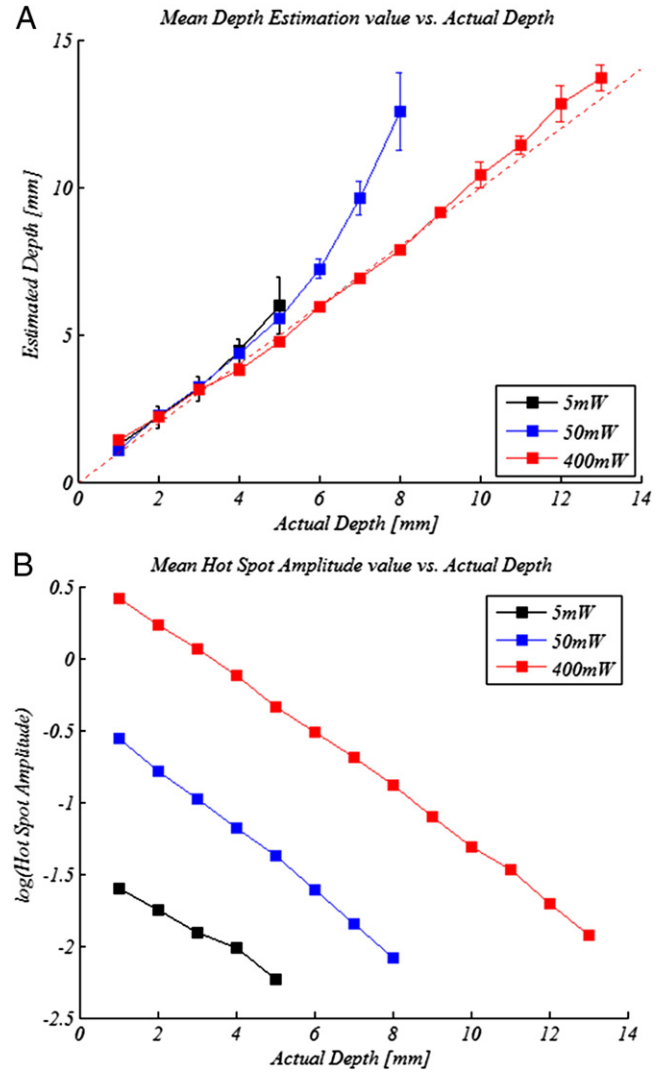


Figure 6. Tumor depth estimation (A) and hot spot amplitude (B), both as a function of depth for three different cases of heat emission power emitted from the tumor phantom: 5 mW (black), 50 mW (blue), and 400 mW (red).

bias, and standard deviation are sufficient, regardless of the tumor depth and its power; however, once the amplitude descends below  $5 \times 10^{-2}$  K, the algorithm performance declines sharply. The depth estimation bias error could be corrected (in a future study) by adding an offset value to the depth estimation according to the measured hot spot amplitude and other parameters.

*Tumor detection sensitivity as a function of power*

As can be seen in Figure 7, for all cases in which the emitted power was 3 mW or higher, the tumor was detected at its correct location for every individual experiment; accordingly, the sensitivity was evaluated as 100% for these cases. As was mentioned before, these results do not necessarily imply that 100% sensitivity can be achieved in a practical clinical scenario. As was noticed in the depth scan experiments, the behavior of the sensitivity function is also nonlinear, with a distinct threshold

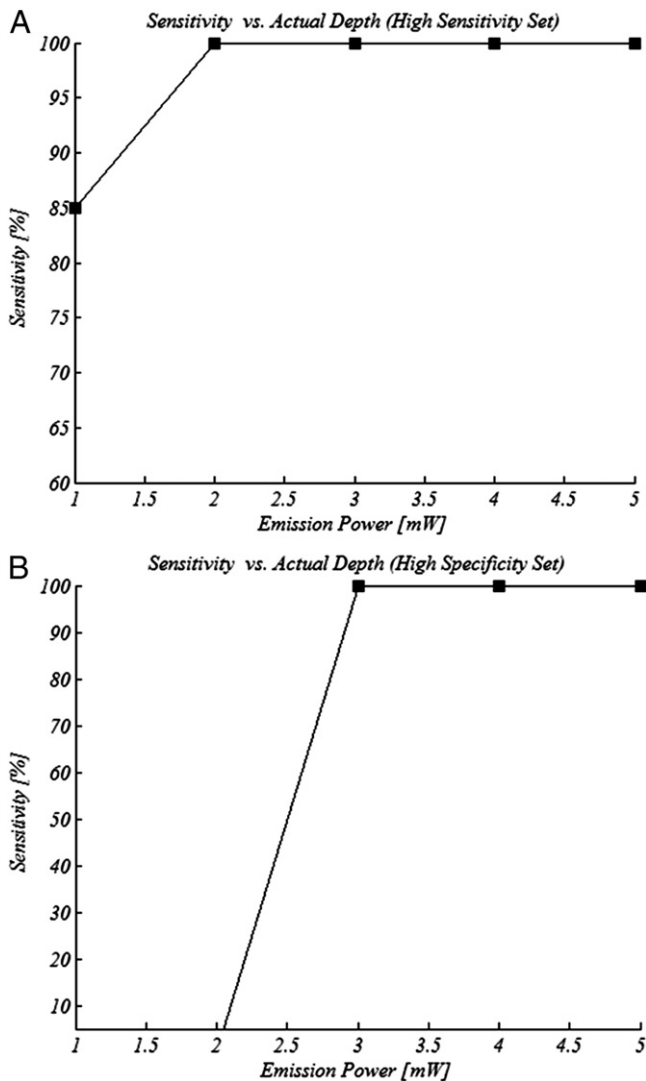


Figure 7. Tumor detection sensitivity as a function of power, for the high-sensitivity parameters set (A) and for the high-specificity parameters set (B), both for a tumor depth of 1 mm.

value. The minimal detectable emitted power for the “high-sensitivity” threshold values is 1 mW; however, in the case of the “high-specificity” threshold set, the tumor was detected only for emitted power of 3 mW or higher.

#### Depth estimation bias and accuracy as a function of power

As can be seen in Figure 8, the bias and standard deviation measurements (Figure 8, A) show that the decrease in hot spot amplitude results in a significant increase in the depth estimation bias and a reduction in the depth estimation accuracy (up to 1 mm bias and  $1.1 \text{ mm} \pm \text{SD}$ ).

#### Specificity test experimental results

For the “high-sensitivity” set, in a total of 148 out of 150 cases, no tumor was detected; accordingly, the specificity was calculated as 98.66%. For the “high-specificity” test, in all 150

cases a tumor was not detected; therefore, the specificity was evaluated as 100%. As was described above, the “cost” of this improved specificity performance is a reduced sensitivity.

#### AMF results

The detection algorithm has managed to detect and locate the MNP-labeled tumor phantom, located 3 mm below the surface, in all cases for both of the parameter sets (Figure 9), which indicates a detection specificity evaluation of 100%. The average hot spot amplitude was  $35.3 \text{ m} \cdot \text{K}$ , the depth estimation bias was  $-0.9 \text{ mm}$ , the depth estimation standard deviation was  $0.445 \text{ mm}$ , and the  $xy$  location standard deviation was  $1.4731 \text{ mm}$ . The results of this experiment verify that a magnetically marked tumor can be detected and located below the tissue surface using the proposed method.

#### Discussion

The results show that malignant tumors can be identified using the proposed TBT approach. The most important conclusion is the ability of this approach to detect tumors emitting extremely low thermal power (as low as 0.5 W) in case the tumor depth is low. As can be seen in Table 1, this thermal power is equivalent to a sub-millimeter (0.5 mm) malignant tumor, under achievable parameters of SAR and particles concentration. This potential detection ability can provide improvements of several orders of magnitude, compared with other cancer detection modalities. It also should be mentioned that in case of low-depth tumors, the effect of blood perfusion (which was not modeled in the current experimental setup) can be neglected; therefore, the experiments can serve as a good clinical feasibility induction for this method.

Another important conclusion concerns the detection specificity of the proposed method. The results show that with correct parameter selection, the method could offer an extremely specific detection; the specificity with the “high-specificity” set was evaluated as 100%. Such high specificity could considerably reduce the false alarm rate in future clinical applications. It should be mentioned that the current setup has not simulated all the expected noises and artifacts that may be present in a real clinical scenario (e.g., natural temperature fluctuation); therefore, further investigation should be done for more conclusive verification of this finding.

Another conclusion concerns the maximal depth at which small tumors can be detected using this method. The experiments have demonstrated a detection of tumor phantom simulating a small tumor ( $<5 \text{ mm}$ ) that was embedded at up to 14 mm below the surface. This was done under the assumption of achievable SAR and particles concentration. It can be assumed that deeper tumors at this size range could be detected by utilizing longer recording time; however, because it reduces the clinical practicality of the method, this issue was not tested. In addition, it will probably be possible to detect larger tumors at greater depths; however, because larger tumors can generally be detected using conventional methods, the issue was also not tested. It is important to mention that unlike low-depth tumor, in the case of deep tumors the blood perfusion plays a more

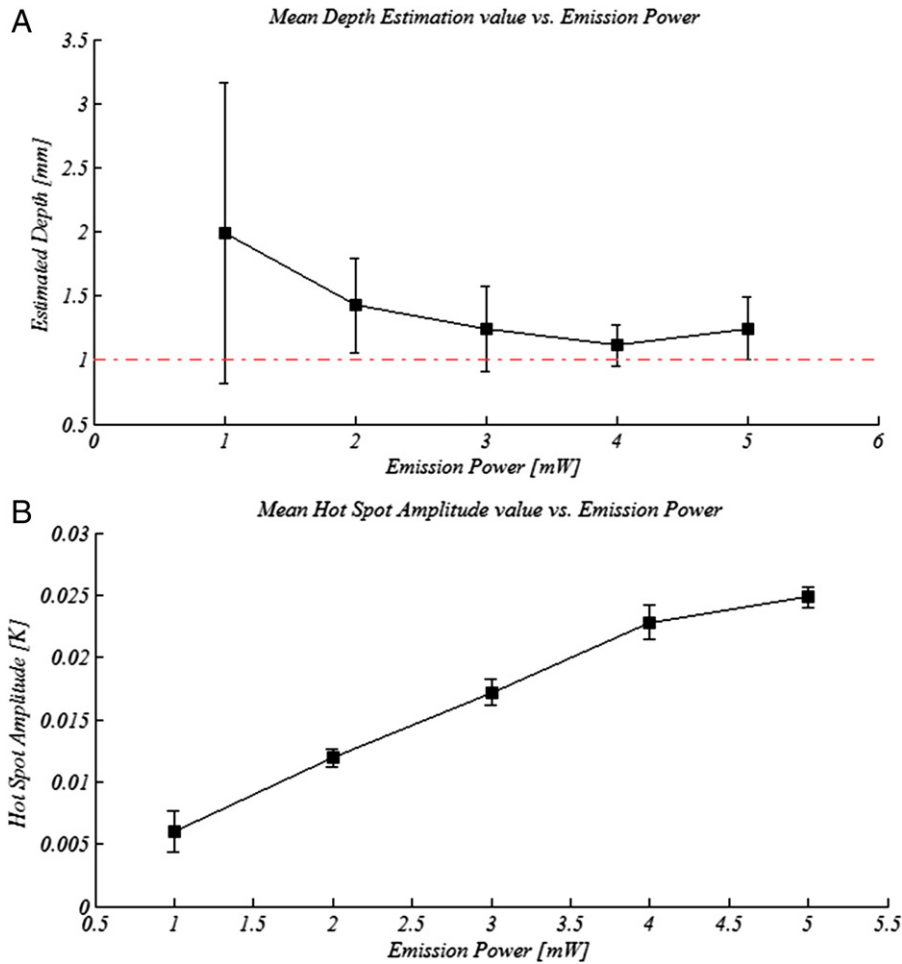


Figure 8. Tumor depth estimation (A) and hot spot amplitude (B), both as a function of emission power for a 1-mm embedded tumor phantom.

significant role; therefore, it is important to model it in the experimental setup and to examine its effect on the detection ability, in that its effect is currently unclear. On the one hand, blood perfusion inside and around the tumor removes heat from the tumor and its surroundings; therefore, it will probably decrease significantly the hot spot amplitude at the surface. On the other hand, local temperature increase in the tumor surroundings can induce a local increase of blood perfusion on a much wider area; this can lead to a significant temperature increase at the surface that could be detected by the detection algorithm. This effect is expected to be significant for depths of a few centimeters; therefore, it could counteract the negative effect of heat removal and potentially could increase the method's ability to detect deep tumors. The role of this hot spot amplification by blood perfusion should be verified in future in vivo experiments.

Although tumor-specific MNPs were previously suggested as MRI tumor markers for cancer detection,<sup>19</sup> the proposed TBT method can potentially perform the detection with much fewer related costs, as well as shorter exam times compared with the expensive and time-consuming MRI scan. In addition, the TBT approach can additionally provide (unlike MRI) functional thermographic information that can be utilized

as an additional diagnostic indicator for cancer. The low equipment and operational costs (compared to MRI and other methods), together with its potential efficacy and safety, can make the proposed TBT method a good candidate for mass cancer screening.

In summary, the proposed TBT method could potentially offer a cost-effective, safe, and sensitive method for early detection of cancerous tumors. An in vitro detection, using this approach, of small embedded tumor phantoms was demonstrated. The results show that the TBT approach can potentially provide a very specific and sensitive detection of small embedded tumors and can achieve significantly improved performance as compared with a conventional thermographic approach. Nevertheless, additional work is still needed to provide a more profound in vivo concept validation of this concept before it could be suggested for future clinical application.

#### Acknowledgments

The authors would like to thank Shlomo Margel from Bar Ilan University for supplying the MNPs that were used in some of the experiments.

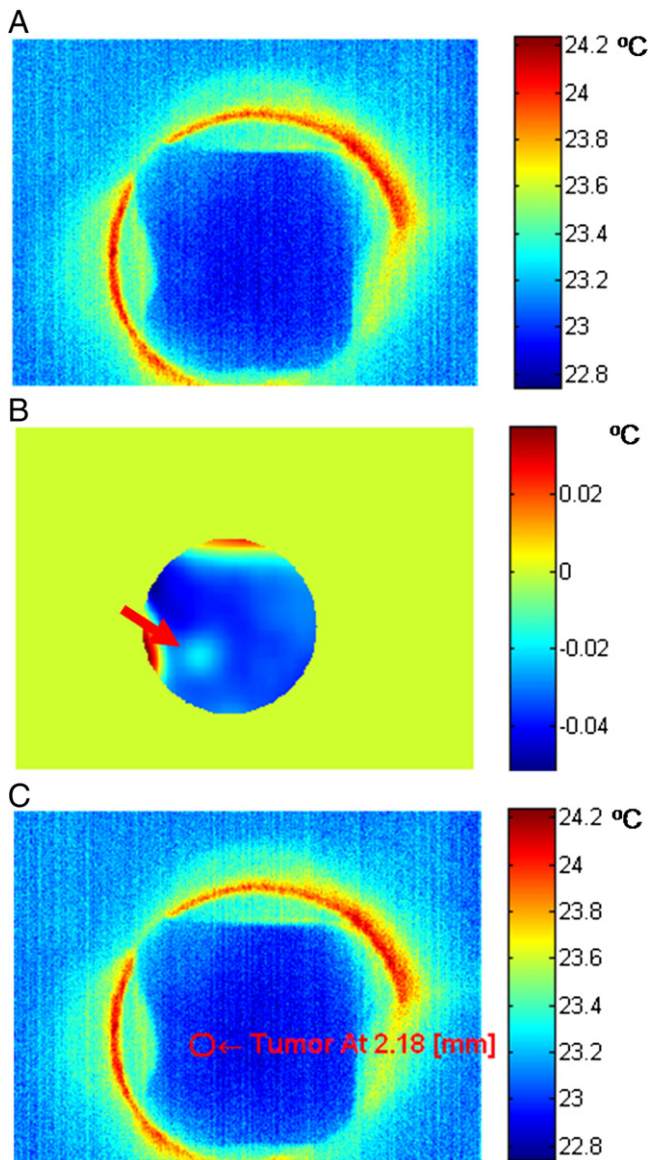


Figure 9. Several stages during detection of an embedded tumor phantom using experimental setup 2. (A) The original image; (B) the preprocessed image with a distinct hot spot (red arrow); (C) the final marked image. (Note: Degrees K = Degrees C + 273.15.)

## References

1. Jemal A, Siegel R, Ward E, Hao Y. Cancer statistics 2008. *CA Cancer J Clin* 2008;58:71-96.
2. Report of the working group to review the National Cancer Institute–American Cancer Society Breast Cancer Detection Demonstration Project. *J Natl Cancer Inst* 1979;62:639-709.
3. Lawson RN. Implications of surface temperature in the diagnosis of breast cancer. *Can Med Assoc J* 1956;75:309-10.
4. William CA. Infrared imaging of the breast. In: Bronzino JD, editor. *Medical devices and systems. The biomedical engineering handbook*. 3rd ed. Boca Raton (FL): CRC Press; 2006.
5. Qi H, Phani TK. Detecting breast cancer from thermal infrared images by asymmetry analysis. In: Bronzino JD, editor. *Medical devices and systems. The biomedical engineering handbook*. 3rd ed. Boca Raton (FL): CRC Press; 2006.
6. Ohashi Y. Applying dynamic thermography in the diagnosis of breast cancer. *IEEE Eng Med Biol Mag* 2000;19:42-51.
7. Kriege MK, Brekelmans CTM, Klijn JGM. MRI screening for breast cancer in women with a familial or genetic predisposition. *Imaging decisions. Magn Reson Imaging* 2005;9:11.
8. Dobson DJ. Magnetic nanoparticles for drug delivery. *Drug Dev Res* 2006;67:55-60.
9. Pankhurst QA, Connolly J, Jones SK, Dobson J. Applications of magnetic nanoparticles in biomedicine. *J Physics D Appl Physics* 2003;36:167-781.
10. Rosensweig RE. Heating magnetic fluid with alternating magnetic field. *J Magn Magn Mater* 2002;252:370-4.
11. Sinha R, Kim GJ, Nie S, Shin DM. Nanotechnology in cancer therapeutics: bioconjugated nanoparticles for drug delivery. *Mol Cancer Ther* 2006;5:1909-17.
12. Goya GF, Grazú V. Magnetic nanoparticles for cancer therapy. *Curr Nanosci* 2008;4:1-16.
13. Shinkai M, Le B, Honda H, Yoshikawa K, Shimizu K, Saga S, et al. Targeting hyperthermia for renal cell carcinoma using human MN antigen-specific magnetoliposomes. *Cancer Sci* 2001;92:1138-45.
14. DeNardo SJ, DeNardo GL, Miers LA, Natarajan A, Foreman AR, Gruettner C, et al. Development of tumor targeting bioprobes ( $^{111}\text{In}$ -chimeric L6 monoclonal antibody nanoparticles) for alternating magnetic field cancer therapy. *Clin Cancer Res* 2005;11:7087s-92s.
15. Le B, Shinkai M, Kitade T, Honda H, Yoshida JUN, Wakabayashi T, et al. Preparation of tumor-specific magnetoliposomes and their application for hyperthermia. *J Chem Eng Jpn* 2001;34:66-72.
16. Hergt HR, Hiergeist R, Hilger I, Kaiser WA, Lapatnikov Y, Margel S, et al. Maghemite nanoparticles with very high AC-losses for application in RF-magnetic hyperthermia. *J Magn Magn Mater* 2004;270:345-57.
17. Pennes HH. Analysis of tissue and arterial blood temperatures in the resting human forearm. *J Appl Physiol* 1948;1:93-122.
18. Duck FA. *Physical properties of tissue: a comprehensive reference book*. New York: Academic Press; 1991.
19. Jaffer FA, Weissleder R. Molecular imaging in the clinical arena. *JAMA* 2005;293:855-62.